

EDGE ARTICLE

[View Article Online](#)
[View Journal](#) | [View Issue](#)Cite this: *Chem. Sci.*, 2025, **16**, 11659 All publication charges for this article have been paid for by the Royal Society of ChemistryReceived 4th February 2025
Accepted 27th May 2025DOI: 10.1039/d5sc00905g
rsc.li/chemical-science

Introduction

Cerium dioxide is an important earth-abundant n-type semiconducting material widely used in catalytic converters,¹ self-cleaning materials, water purification,² catalytic antioxidants in medicine,^{2,3} and (photo)catalysis, with recent interest in the use of ultrasmall (<3 nm) CeO₂ particles.^{4,5} CeO₂ adopts the fluorite structure in which each Ce is coordinated by eight O atoms in a cubic coordination geometry, with Ce–O distances of 2.37 Å and Ce···Ce distances of 3.87 Å. Whilst the majority of Ce atoms exist in the Ce(IV) oxidation state, the material naturally exists in a non-stoichiometric form with formula CeO_(2-x), with oxygen vacancies and associated Ce(III) sites that are concentrated on the surface of particles.⁵⁻⁸

To effectively use these systems for photocatalytic applications it is essential to have a good understanding of the electronic structure and light absorption properties. The major electronic excitation in CeO₂ is an oxygen 2p (valence band) to cerium 4f charge transfer (oxygen to metal charge transfer, OMCT) transition.⁹ The contracted empty 4f orbitals of Ce are localized (atomic-like), leading to a very narrow ‘band’ of energy states.¹⁰⁻¹² Band gap charge transfer transitions are responsible

Photoabsorption of 1–2 nm molecular Ce-oxo nanoclusters *versus* ceria: intervalence charge transfer but no size effects†

Stephen E. Brown  and Sebastian D. Pike  *

The absorption spectra of a series of Ce-oxo clusters (molecular nanoparticles) with sizes ranging from 3 to 100 Ce atoms per cluster are reported. The O 2p to Ce 4f charge-transfer absorption onset in these systems is unaffected by size and almost identical to that of 5 nm CeO_(2-x) particles and other Ce based materials such as the metal–organic framework Ce–UiO-66. This clearly demonstrates that in CeO₂ based systems, with highly localized 4f LUMO orbitals, quantum confinement effects are not influential on electronic structure. Importantly, this allows the use of ultrasmall ceria particles in (visible light) photochemical applications without detrimental band-gap enlarging size-effects. Changes in colour in CeO₂ materials and these Ce-oxo clusters are instead clearly attributed to the presence of (defective) surface sites. Surface Ce(III) sites in mixed-valence clusters contribute a Ce(III)/Ce(IV) intervalence charge transfer transition in the visible region, which affects their colour. Ce₂₄ clusters with a range of aliphatic and aromatic carboxylate ligands are studied, to compare the effect of surface ligands on the electronic structure. Ligand influence on the absorption spectra is only observed when highly conjugated (naphthyl) or strongly electron donating substituents (anisole or aniline) are present.

for the photoactivity in wide-band gap metal oxide semiconductors and can lead to effective charge separation and redox reactivity. Following photoexcitation of CeO_(2-x), the excited electron rapidly (<2 ps) couples with phonons (vibrations) to generate a small polaron state (distorted lattice directly around the generated Ce³⁺ state), and conductivity within CeO_(2-x) is believed to occur *via* a small polaron hopping mechanism.^{10,13,14}

The colour of ceria materials varies from white to pale yellow, depending on the synthetic process, with varying values for the band gap reported (indirect gap 2.5–3.3 eV, direct gap 3.2–3.6 eV), noting that the method of analysis can give different values.^{10,15–17} Yellow colours imply the ability to absorb blue light, *e.g.* lower energy photons can perform electronic excitations. These lower energy processes are suggested to involve defective surface sites,¹⁸ sometimes termed the ‘Urbach tail’, attributed to surface disorder, and may be dependent on Ce³⁺ content.^{10,12} The presence of Ce(III) sites, with a 4f¹ electron configuration, may affect the electronic spectra, as the 4f electrons may be excited using low energy (visible light) *via* intervalence charge transfer processes.⁹ Further excitation from a 4f¹ (polaron) state to the empty 5d band is expected to require higher energies of 3.2–3.7 eV in the UV range.¹⁰ In this article the spectra of defective nano-ceria is compared with well-defined molecular Ce-oxo clusters, where any ‘defects’ are clearly resolved in the precise atomic structure, providing a more detailed understanding of these phenomena.

Department of Chemistry, University of Warwick, CV4 7AL, Coventry, UK. E-mail: sebastian.pike@warwick.ac.uk

† Electronic supplementary information (ESI) available. CCDC 2418676–2418679, 2418699–2418701 and 2418814. For ESI and crystallographic data in CIF or other electronic format see DOI: <https://doi.org/10.1039/d5sc00905g>

With increasing interest in ultrasmall (high surface-area-to-volume) nanomaterials, it is important to understand how the properties of materials change with size. Nanoscaling commonly effects the electronic properties of a semiconductor material, as the valence and conduction bands becomes less continuous and narrower through the process of quantum confinement.¹⁹ The result of quantum confinement is typically an enlargement of the band gap and blue-shift of the absorption onset. Quantum confinement effects are expected to occur once the size of a nanoparticle shrinks below the exciton Bohr-radius of the material. For some low band gap materials, such as CdS, this effect is observed over a wide size range (particles <20 nm) resulting in a large range of band gaps for differently sized particles. The exciton Bohr-radius of $\text{CeO}_{(2-x)}$ is not well defined, however, in other semiconductors with similar band-gaps size effects are only observed at very small sizes ($\text{ZnO} < 7$ nm, $\text{TiO}_2 < 2$ nm).^{20,21} To date, reports of quantum confinement effects in $\text{CeO}_{(2-x)}$ are inconsistent, with some reports suggesting a blue shift in small nanoparticles (e.g. 2.9 eV for ~ 6 nm particles shifting to ~ 3.1 eV for 3–4 nm particles, by measuring the indirect allowed transition),^{22,23} whilst other reports indicate a slight red-shift in the band gaps relative to bulk $\text{CeO}_{(2-x)}$ for ultrasmall particles (e.g. 2.5 eV for 6–8 nm particles¹⁷).¹² Other studies suggest no quantum confinement effect in fully oxidized CeO_2 nanoparticles, ranging from ~ 7 nm to ~ 1.5 nm.^{24,25} The consequence of an unchanging absorption onset with size is significant, as improving the surface-area by nanoscaling $\text{CeO}_{(2-x)}$ would not result in reduced solar light absorption.

A further study shows that the optical properties of ~ 2 nm $\text{CeO}_{(2-x)}$ nanoparticles quantitatively correlate with the value of x and the valence state of the Ce atoms.²⁶ The optical density of the particles decreases (bleaches) as they become reduced, resulting in a weaker absorbance (which could erroneously be assigned as a blue shift in onset). These results are confirmed by other reports, which suggest that the optical density decreases as Ce(III) forms at the surface, essentially decreasing the volume of the CeO_2 core.^{24,27} It is also noteworthy that nanoscaling of $\text{CeO}_{(2-x)}$ leads to an increase in the lattice parameter once below 20 nm (0.45% larger at 6 nm), which may be caused by an increased proportion of Ce(III) + oxygen vacancies or due to increased strain at the surface sites which coordinate with adsorbed species.^{12,28}

Considering the variable chemical state of $\text{CeO}_{(2-x)}$ nanoparticles *via* their (size-dependent) interaction with local environment, it may not be sensible to apply a classical interpretation of quantum confinement which considers a change in properties on shrinking volume of a consistent chemical state.²⁹ It is also noteworthy that particle shape and well-defined facets in larger nanoparticles of CeO_2 (e.g. 9–100 nm) may also effect their UV/visible absorption spectra and reported band gap.^{30,31}

One challenge in characterising nanoparticle systems is their inherent polydispersity and a lack of understanding at the atomic level. In contrast, precisely defined molecular metal-oxo clusters provide exceptional understanding of atom connectivity in monodisperse systems. Recently, fascinating nanoscale

Ce-oxo clusters (or molecular nanoparticles) have been discovered, with up to 100 Ce atoms (2.4 nm Ce–O maximum core diameter).^{32–37} These remarkable structures exhibit the CeO_2 fluorite lattice in their Ce–O cores (Fig. S1†) which is then supported by surface organic ligands such as anionic carboxylates and neutral N-donor ligands (similar to surfactant stabilized nanoparticles).³⁸ Reported structures exhibit differing degrees of Ce(III) occupancy varying from 0–40% of Ce atoms,^{34,39} identified from bond length analysis (bond valence sum calculations) of their molecular crystal structures. Furthermore, even smaller Ce-oxo clusters, such as $\text{Ce}(\text{IV})_6\text{O}_4(\text{-OH})_4(\text{carboxylate})_{12}$,⁴⁰ or similar,^{41,42} are highly relevant for this discussion, especially due to their common use in important metal–organic framework (MOF) structures (e.g. Ce–UiO-66) and in photocatalysis.^{40,43–46} In these molecular systems, almost the entirety of the structure is ‘surface’ and ligand orbitals significantly contribute to the electronic structure.⁴⁷ Therefore, it is important to consider whether the ligand can introduce mid-gap (HOMO) orbitals which may reduce the HOMO–LUMO gap (which is the molecular equivalent of the band gap), this is more likely for ligands with conjugated structures with high lying filled orbitals, and such ligands are commonly studied for their relevance to dye-sensitised materials.^{48,49} Ce-oxo clusters ranging from Ce_6 – Ce_{38} and bulk CeO_2 have been previously studied by X-ray absorption spectroscopy, to show the transition from a surface dominated molecule to a molecular nanoparticle, containing core Ce atoms in a cubic crystal field more closely resembling CeO_2 .³⁷ This indicated the average crystal field splitting (ΔO_h) of the 5d orbitals increases with particle size, but interestingly the lower energy 2p–4f X-ray absorptions were consistent across the size range, indicating the energy of the 4f orbitals remains consistent.

In this study we compare the electronic absorption (UV/visible) spectra of a range of differently sized Ce-oxo clusters varying from 3–100 Ce atoms which have differing supporting ligands, shapes and Ce(IV)/Ce(III) ratios and contrast these with typical $\text{CeO}_{(2-x)}$ materials and MOFs, all using consistent methods. The results show a negligible change in the oxygen to metal (Ce 4f) charge-transfer onset across all size ranges, with all materials maintaining an indirect absorption onset of 2.6–2.9 eV. The lack of quantum confinement contrasts to studies of other metal-oxides,^{20,50} and is of relevance to findings which suggest that highly localized charge transfer excitons can be formed in metal oxide materials.⁵¹

Results and discussion

Spectroscopic results

A series of Ce-oxo clusters were prepared as crystalline materials using literature routes, ranging from small cerium-(oxo)-alkoxide species $[\text{Ce}(\text{IV})_3\text{O}(\text{O}^t\text{Bu})_{10}]$ (Ce_3),⁵² through high symmetry $[\text{Ce}(\text{IV})_6\text{O}_4(\text{OH})_4(\text{O}_2\text{C}^t\text{Bu})_{12}]$ (Ce_6),³⁵ to larger ‘molecular nanoparticles’ $[\text{Ce}_{22}(\text{IV})\text{Ce}_2(\text{m})_4\text{O}_{28}(\text{OH})_8(\text{O}_2\text{CPh})_{30}(\text{py})_4]$ ($\text{Ce}_{24}^{\text{Ph}}$),^{32,33} $[\text{Ce}_{38}(\text{IV})\text{Ce}(\text{m})_2\text{O}_{56}(\text{OH})_2(\text{O}_2\text{CMe})_{44}(\text{MeCO}_2\text{H})_2(\text{py})_4]$ (Ce_{40})³² and $[\text{Ce}(\text{IV})_{92}\text{Ce}(\text{m})_8\text{O}_{149}(\text{OH})_{18}(\text{O}_2\text{CPh})_{60}(\text{H}_2\text{O})_{20}](\text{O}_2\text{CPh})_8(\text{NO}_3)_8$ (Ce_{100})³³ (Fig. 1 and S3–S11, Table S2†). Structures were confirmed by single-crystal X-ray diffraction and bulk powders contain the

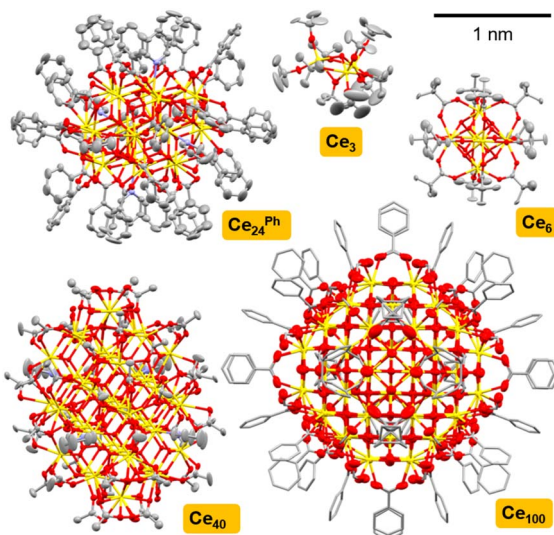


Fig. 1 Single crystal X-ray structures of Ce_3 ,⁵³ Ce_6 ,⁵⁴ $\text{Ce}_{24}^{\text{Ph}}$,³⁴ Ce_{40} ,³² Ce_{100} ³³ to scale. Ellipsoids at 50% probability, H-atoms omitted for clarity, C atoms shown as capped sticks in Ce_{100} . Ce = yellow, O = red, N = blue, and C = grey.

expected C, H, N content by elemental analysis (Table S1†) (note that purity of air-sensitive Ce_3 was instead determined *via* solution NMR spectroscopy, Fig. S3†). The PXRD pattern of Ce_6 implies a trace impurity of larger clusters may also be present (Fig. S5†). In Ce_3 the Ce atoms adopt octahedral coordination geometries (face-sharing octahedra, Ce–Ce distances 3.527 Å), whilst square antiprismatic (eight-coordinate) geometry is found in Ce_6 (edge-sharing square antiprisms, Ce–Ce distances 3.764–3.769 Å), and the larger clusters all mimic the cubic coordination geometry of the fluorite structure at their core, although surface Ce(iv) sites vary in coordination geometry (for $\text{Ce}_{24}^{\text{Ph}}$, Ce–Ce distances range 3.7–3.9 Å).^{32,33} In $\text{Ce}_{24}^{\text{Ph}}$, Ce_{40} and Ce_{100} Ce(III) atoms are also present, and these have ten-coordinate geometries and are found exclusively on the cluster surface.^{32,33}

To expand this series in order to evaluate the effect of surface ligands, a set of novel Ce_{24} clusters were prepared with the same overall formula as $\text{Ce}_{24}^{\text{Ph}}$ but with different carboxylate ligands (O_2CR : R = $n\text{-C}_3\text{H}_7$, $\text{Ce}_{24}^{\text{But}}$; $n\text{-C}_5\text{H}_{11}$, $\text{Ce}_{24}^{\text{Hex}}$; $p\text{-C}_6\text{H}_4\text{Me}$, $\text{Ce}_{24}^{\text{PhMe}}$; $p\text{-C}_6\text{H}_4^t\text{Bu}$, $\text{Ce}_{24}^{\text{Ph}^t\text{Bu}}$; $p\text{-C}_6\text{H}_4\text{F}$, $\text{Ce}_{24}^{\text{PhF}}$; $p\text{-C}_6\text{H}_4\text{OMe}$, $\text{Ce}_{24}^{\text{PhOMe}}$; $p\text{-C}_6\text{H}_4\text{NH}_2$, $\text{Ce}_{24}^{\text{PhNH}_2}$; 1-naphthyl, $\text{Ce}_{24}^{\text{1Nap}}$, 2-naphthyl, $\text{Ce}_{24}^{\text{2Nap}}$). All structures form with isostructural Ce_{24} cores (Fig. 2, 3 and S12–S17†). Where enough ligand information could be resolved in the single crystal X-ray structure ($\text{Ce}_{24}^{\text{Ph}}$, $\text{Ce}_{24}^{\text{PhMe}}$, $\text{Ce}_{24}^{\text{PhF}}$, $\text{Ce}_{24}^{\text{PhOMe}}$, $\text{Ce}_{24}^{\text{1Nap}}$, $\text{Ce}_{24}^{\text{2Nap}}$) bond valence sum analysis confirmed the expected location of two surface Ce(III) sites on opposite ends of the cluster core (Fig. 2 and 3, Tables S2–S7†).⁵⁵ The structures with aliphatic carboxylates, $\text{Ce}_{24}^{\text{But}}$ and $\text{Ce}_{24}^{\text{Hex}}$ demonstrate that benzoate ligand pi interactions are not essential for structure assembly. Assessing bulk purity of these paramagnetic compounds (which are typically insoluble in inert solvents) is challenging, especially as crystallinity is lost upon drying the samples (see Fig. S19†), however, elemental analysis of these new compounds is mostly

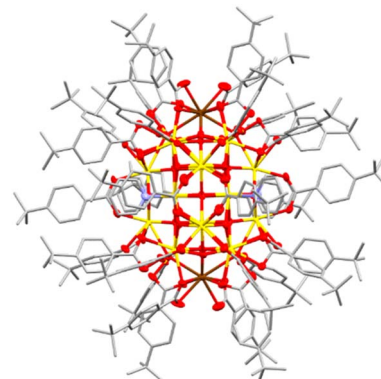


Fig. 2 Single crystal X-ray structure of $\text{Ce}_{24}^{\text{Ph}^t\text{Bu}}$. Ellipsoids at 50% probability, H-atoms omitted for clarity, C atoms shown as capped sticks. Ce(iv) = yellow, Ce(III) = brown, O = red, N = blue, and C = grey.

in excellent agreement with the expected formula (Table S1†). Further analysis of bulk purity and near IR spectroscopy is included in the ESI.†

The synthetic process that generates these Ce_{24} clusters consists of dissolving 24 equivalents of carboxylic acid in pyridine/water (10 : 1 ratio), generating a basic solution of pyridinium carboxylate. To this, four equivalents of $\text{Ce}(\text{III})(\text{NO}_3)_3(\text{H}_2\text{O})_6$ is added, most likely forming $[\text{Ce}(\text{III})(\text{carboxylate})_3]_x$ structures in solution (ESI Note 1†), it is crucial that these species remain solubilized at this stage.⁵⁶ Next, one equivalent of $(\text{NH}_4)_2\text{Ce}(\text{IV})(\text{NO}_3)_6$ is added and the reaction mixture layered with acetone. The reaction solution slowly darkens from yellow to brown and Ce_{24} compounds crystallise. The crystalline yield is typically below 20% total Ce (or <100% Ce(iv) reagent), therefore, we hypothesise that the $[\text{Ce}(\text{III})(\text{carboxylate})_3]_x$ solution is important for allowing the clusters to form, but that the predominantly Ce(iv) clusters are mostly built from Ce(iv) atoms from $(\text{NH}_4)_2\text{Ce}(\text{IV})(\text{NO}_3)_6$.

The diffuse reflectance UV/visible spectra of a range of commercially available ceria materials were collected (Fig. 4), these materials all display expected powder-X-ray diffraction

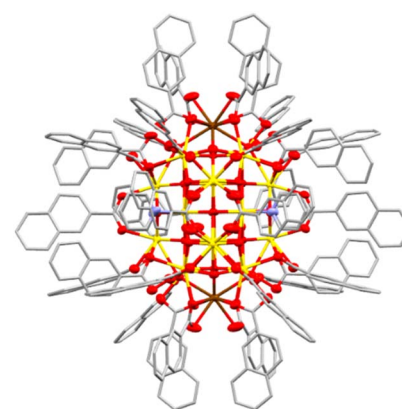


Fig. 3 Single crystal X-ray structure of $\text{Ce}_{24}^{\text{2Nap}}$. Ellipsoids at 50% probability, H-atoms and non-coordinated pyridine molecules omitted for clarity, C atoms shown as capped sticks. Ce(iv) = yellow, Ce(III) = brown, O = red, N = blue, and C = grey.



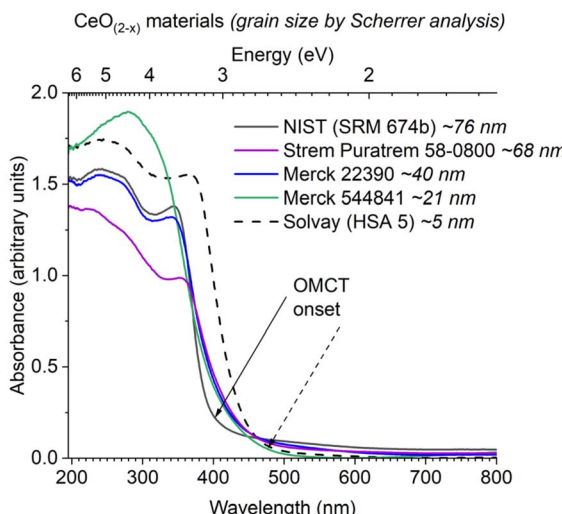


Fig. 4 Diffuse reflectance UV/vis spectra of commercial ceria (nano)materials. Arrows show calculated onset value from Tauc's analysis for largest and smallest particles.

patterns for ceria (Fig. S22, Table S8†), and no other metals (except trace Al) were detected above the detection limit of X-ray fluorescence spectroscopy (Table S9†). In this study all absorption onsets are calculated using Tauc's method of plotting $(F(R_\infty)h\nu)^{1/n}$ vs. $h\nu$, with $n = 3$ for an indirect forbidden (2p to 4f) process (Fig. S23†), it is worth noting the potential error ($\sim \pm 0.1$ eV) in these calculations, and always worth visually comparing collected spectra rather than only the 'onset' value.⁵⁷ The data demonstrates the differing absorption onsets in ceria materials (Fig. 4); the NIST standard CeO_2 (~ 75 nm grain size, low defect density) is white with an onset of 3.1 eV. In contrast, a high surface area (HSA) sample (Solvay HSA 5, ~ 5 nm particles) is yellow and displays a red-shifted onset at 2.6 eV. Other 'standard' ceria samples are pale yellow and show similar onsets to the HSA sample, calculated to be 2.6–2.8 eV, but with a spectral profile which more resembles the NIST sample at higher energies. Therefore, we suggest the highly crystalline NIST sample and the high surface area HSA sample act as the outliers, with 'standard' ceria behaving like a defective version of the NIST sample.

The absorption spectra of Ce-oxo clusters was collected and compared to 5 nm ceria (Fig. 5). The spectra clearly show that the major OMCT excitation (with 'band-gap like' O 2p to Ce 4f character) begins at very similar onset values for all of these compounds (range; 2.7–2.8 eV, Table S10†), and the spectra are remarkably similar to HSA ceria. A small difference is noted for yellow/orange Ce_3 (onset 2.4 eV) which has only oxo and alkoxide ligands and a different coordination geometry at Ce.

Ce_3 and pale yellow Ce_6 only have absorptions in the OMCT region, noting that these are only expected to contain Ce(iv) sites, therefore, there is no possibility of intervalence charge transfer (IVCT), 4f → 5d or 4f → ligand excitations in these cases. In contrast, the molecular nanoparticles $\text{Ce}_{24}^{\text{Ph}}$, $\text{Ce}_{24}^{\text{But}}$, Ce_{40} and Ce_{100} are brown, with additional absorptions (centered at ~ 525 –550 nm) at lower energies than the OMCT band. This

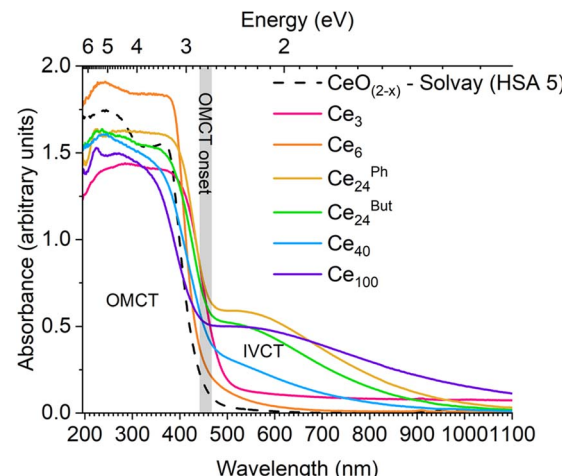


Fig. 5 Diffuse reflectance UV/vis spectra of Ce-oxo clusters in comparison to high surface area $\text{CeO}_{(2-x)}$. Note the steep increase, attributed to the OMCT absorption, begins at a similar value for all solid compounds except Ce_3 (onset region determined by Tauc's analysis highlighted in grey).

absorption in the visible region correlates with the Ce(III) content in these mixed valence compounds; $\text{Ce}_{24}^{\text{Ph}}$, $\text{Ce}_{24}^{\text{But}}$, and Ce_{100} are reported to have 8% Ce(III), whilst Ce_{40} has 5% Ce(III) and consequently has a weaker absorption in the visible region. The nature of these visible excitations is attributed to a metal to metal charge transfer process, *i.e.* a Ce(III)/Ce(IV) IVCT. Visible-light IVCT excitations from Ce(III) sites have previously been proposed as the cause for darkening of CeO_2 @ethylene glycol nanoparticles under UV irradiation, with colour bleaching when subsequently heated under air.⁵⁸ To confirm that this excitation is not 4f to ligand (carboxylate/pyridine π^*) based (*i.e.* metal to ligand charge transfer (MLCT)), or 4f to 5d, the coordination polymer $[\text{Ce}(\text{III})(\text{O}_2\text{CCH}_2^{\text{t-Bu}})_3\text{Py}]_\infty$ was studied. This compound contains only 9-coordinate Ce(III) sites that are coordinated to carboxylate and pyridine ligands. $[\text{Ce}(\text{O}_2\text{CCH}_2^{\text{t-Bu}})_3\text{Py}]_\infty$ exhibits a charge transfer absorption onset at 2.7 eV (N.B. commercial $\text{Ce}(\text{acetate})_3$ hydrate absorbs from 3.0 eV), but no further absorptions are observed in the visible region, discounting the presence of 4f MLCT or 4f–5d excitations (Fig. S24–S27†) in Ce(III) only systems.

To further characterize these compounds and the IVCT excitation, the solution UV/visible spectrum of the readily soluble compounds Ce_3 and $\text{Ce}_{24}^{\text{PhBut}}$ were collected in toluene, and THF for the latter (Ce_3 0.9 mM, $\text{Ce}_{24}^{\text{PhBut}}$ 1.3 mM, Fig S28 and S29†). The OMCT onset in the solution spectrum of $\text{Ce}_{24}^{\text{PhBut}}$ shows good agreement to the solid-state data (solid, 2.69 eV; toluene, 2.71 eV; THF, 2.69 eV, Fig. S30†), which is also very similar to that of Ce_3 in solution (toluene, 2.69 eV). The onset of Ce_3 is blue-shifted relative to when in the solid-state, perhaps due to its very small size and the significant structural changes possible on solvation (Fig. S31†). The $\text{Ce}_{24}^{\text{PhBut}}$ data is similar to previous reports of the solution UV spectra of $\text{Ce}_{24}^{\text{Ph}}$ and Ce_{100} in DMF solvent, but with greater confidence that THF or toluene do not partake in any redox reactivity or structural rearrangement.³³ The IVCT band appears as a weak



feature (e^{\max} : toluene, $100 \text{ M}^{-1} \text{ cm}^{-1}$; THF, $140 \text{ M}^{-1} \text{ cm}^{-1}$) in the solution spectrum of $\text{Ce}_{24}^{\text{PhtBu}}$, consistent with the pale brown colour of the solution (Fig. 6 and S28†), and requires a mM concentration to be observed – noting that weaker peaks are more prominent in non-linear solid-state UV/vis absorption data in comparison to the linear absorption scale for solution data. Gaussian peaks were fit to the OMCT and IVCT regions of the spectra suggesting the IVCT signal is somewhat dependent on solvent (Fig. S32,† THF, max. 513 nm, FWHM 288 nm; toluene, max. 555 nm, FWHM 220 nm). This broad, weak, solvent-polarity dependent feature in the visible region is consistent with a Robin–Day class II system, in which there is some localisation of valence character in the system but a low activation barrier for interconverting between valence states. This agrees with the bond valence sum analysis of these (low-symmetry) Ce_{24} compounds, in which surface sites corresponding to Ce(III) are identified (Tables S2–S7†). In higher symmetry Ce-oxo clusters, the location of well-defined Ce(III) sites is less obvious, and these may be better described as Robin–Day class III systems, with lower energy IVCT transitions.^{36,59} IVCT in lanthanide species is rare, with few clearly defined examples of M(III)/M(IV) IVCT,^{36,59,60} however, the UV/visible spectrum of intermediate-valence $[\text{Ce}_2(\text{IO}_3)_6(\text{OH}_{0.44})]$ shows a similar broad feature at 625 nm,⁵⁹ and the mixed valence cluster $\text{Ce}(\text{III})_4\text{Ce}(\text{IV})_6\text{O}_8(\text{acac})_{14}(\text{CH}_3\text{O})_6(\text{CH}_3\text{OH})_2$, with 40% Ce(III) displays a strong broad feature in its solid-state UV/vis spectrum. Furthermore, recent interest in M(III)/M(II) systems (e.g. f_{13}/f_{14} configurations in Yb systems) also show broad spectral features (e^{\max} $258 \text{ M}^{-1} \text{ cm}^{-1}$ at 600 nm, and e^{\max} $150 \text{ M}^{-1} \text{ cm}^{-1}$ at 725 nm).^{61,62} The four Ce(III)…Ce(IV) distances in $\text{Ce}_{24}^{\text{PhtBu}}$ range $3.73\text{--}3.80 \text{ \AA}$. A (partial) metal–metal bond is identified in a mixed-valence molecule with Dy(II)–Dy(III) distance of 3.71 \AA ,⁶³ noting that this bond forms from the large 5d orbitals, in contrast, molecules with Yb(II)…Yb(III) distances of 2.95 and 3.58 \AA , with only f-orbital occupancy, do not exhibit metal–metal bonds,^{61,62} and, therefore, we do not expect any 4f-based metal–metal bonding in these M(III)/(IV) oxo clusters.

We hypothesised that replacing the two Ce(III) sites in $\text{Ce}_{24}^{\text{PhtBu}}$ with La(III) (without an f electron) should remove the IVCT band

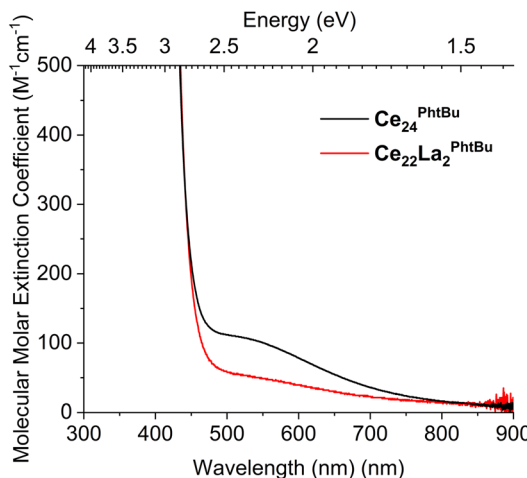


Fig. 6 Solution UV/vis spectra of $\text{Ce}_{24}^{\text{PhtBu}}$ and $\text{Ce}_{22}\text{La}_2^{\text{PhtBu}}$.

and result in a yellow compound. The synthetic process was repeated but using $\text{La}(\text{NO}_3)_3(\text{H}_2\text{O})_6$ instead of $\text{Ce}(\text{III})(\text{NO}_3)_3(\text{H}_2\text{O})_6$, whilst retaining $(\text{NH}_4)_2\text{Ce}(\text{IV})(\text{NO}_3)_6$ as the Ce(IV) source. The resultant solution remained yellow, without darkening to brown, and produced yellow crystals which gave the expected single crystal structure for $\text{Ce}_{24}^{\text{PhtBu}}$. Inductively coupled plasma optical emission spectroscopic analysis of the product revealed a good match for the expected La and Ce content in a cluster with formula $[\text{Ce}_{22}(\text{IV})\text{La}_2(\text{III})_4\text{O}_{28}(\text{OH})_8(\text{O}_2\text{CC}_6\text{H}_4\text{Bu})_{30}(\text{py})_4]$, $\text{Ce}_{22}\text{La}_2^{\text{PhtBu}}$, (La wt%, found 3.15%, calc. 2.90%; Ce wt%, found 30.3%, calc. 32.19%). Solution UV-visible spectroscopy confirmed that the IVCT band for $\text{Ce}_{22}\text{La}_2^{\text{PhtBu}}$ was significantly reduced in this mixed metal compound, consistent with the requirement for Ce(III) for the IVCT absorption (Fig. 6). The same approach was also used to prepare ‘ $\text{Ce}_{22}\text{La}_2^{\text{Ph}}$ ’ as a yellow material (ESI Note 3†).

Due to the high surface content in these compounds, ligand effects are surely important. Mashima and co-workers previously calculated the HOMO of acetate capped Ce_6 clusters $[\text{Ce}_6\text{O}_4(\text{OH})_4(\text{O}_2\text{CR})_{12}]$ to be composed of a combination of oxo, hydroxo and carboxylate O orbitals, whilst in the benzoate analogue the phenyl pi orbitals become the HOMO states, but with the O-based orbitals only 0.1 eV lower in energy. In both cases the Ce 4f orbitals contribute to the LUMO states, and the major contribution to the absorption spectrum is O 2p to Ce 4f charge transfer (OMCT). In our study, switching between benzoate and aliphatic carboxylates has no effect on the absorption spectrum, confirming that the pi system of benzoate does not play a major role. Furthermore, the similarity of Ce_3 , which only has oxo and alkoxide ligands, is consistent with an O centered HOMO state without requirement for carboxylate.

The impact of substituents in the *para* position of benzoate was probed, along with extending the pi system to naphthoate ligands (Fig. 7 and S33†). The OMCT absorption onset remains similar for electron withdrawing ($\text{Ce}_{24}^{\text{PhF}}$, 2.7 eV) or weakly donating ($\text{Ce}_{24}^{\text{PhMe}}$, 2.7 eV; $\text{Ce}_{24}^{\text{PhtBu}}$, 2.7 eV) *para* substituents. However, the absorption becomes slightly shifted for moderately donating ($\text{Ce}_{24}^{\text{PhOMe}}$, 2.5 eV) substituents; and is significantly different for the strongly donating *para*-aminobenzoate

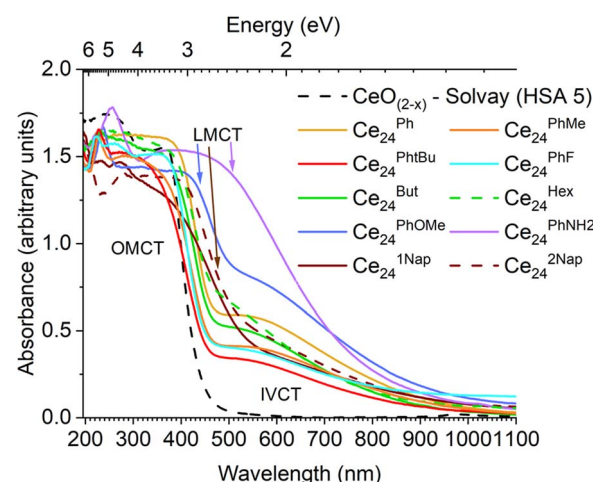


Fig. 7 Diffuse reflectance UV/vis spectra of Ce_{24} -oxo clusters in comparison to high surface area $\text{CeO}_{(2-x)}$.



ligand ($\text{Ce}_{24}^{\text{PhNH}_2}$, 1.2 eV, dark red colour), and is now better termed ligand to metal charge transfer (LMCT). Using larger conjugated pi systems in the naphthoate clusters, also causes a lower energy LMCT onset ($\text{Ce}_{24}^{\text{1Nap}}$, 2.3 eV, $\text{Ce}_{24}^{\text{2Nap}}$, 2.4 eV), in these scenarios the ligand pi system is likely to contribute significantly to the HOMO and/or LUMO. These are well known ligand effects, used in dye sensitised metal oxide materials and MOFs, and allow for tailoring of the visible light absorption properties, but with impact on the location and redox potentials of photoexcited charges.^{40,47,48,64,65}

Finally, to consider the effect of double ended carboxylate linkers, the spectrum of Ce_6 was compared with the MOF Ce-UiO-66 in which the pivalate ligands are replaced with terephthalate linkers (Fig. 8).^{43,48} The MOF exhibits a similar absorption onset, if slightly blue shifted, to the individualised cluster (Ce-UiO-66, 2.9 eV, Ce_6 , 2.7 eV), however, it is noteworthy that literature absorption onset values for Ce-UiO-66 vary (down to 2.5 eV) and show dependence on the amount of defects in the MOF.^{48,66} This batch of MOF, prepared in DMF but without added modulators, has been previously reported to have 22% missing linkers,⁶⁷ the spectra shows a tail into the visible region, consistent with previously reported defective Ce-UiO-66.^{43,66} This implies the presence of Ce(III) defects in the sample that accompany missing linkers and that contribute visible light IVCT contributions to the spectrum.

Discussion

The OMCT absorptions of the Ce_6 – Ce_{100} clusters are almost identical to ~5 nm (HSA ceria) nanoparticles. Whilst the presence of an 'Urbach tail' (from defective surface sites) is used to explain the visible absorption in ceria, this cannot be used for well-defined crystalline molecular systems. Instead, the surface sites and oxidation states are well described, allowing for a greater level of understanding of the excitations involved.

It is remarkable that the OMCT excitation in this range of clusters and nanomaterials retains at a consistent absorption onset. It might be expected that as the particles become smaller,

due to a diminishing number of atomic orbitals contributing to the valence and conduction bands, the bands would become more discreet (molecule like) and, therefore, narrower, resulting in a larger band gap (OMCT onset) as is observed in other metal oxides. In CeO_{2-x} the lowest unoccupied energy states are built from combinations of contracted 4f orbitals. These 4f orbitals are not strongly affected by crystal field, which may explain similarities between species with different coordination geometries.³⁷ Since adjacent 4f orbitals overlap poorly, the range of energy states from in and out of phase combinations of these 4f orbitals may be very small, essentially leading to a series of near degenerate energy, rather localized, states. Upon reducing the number of contributing 4f states, these energies remain close to unchanged, so that the lowest unoccupied energy states remain similarly positioned for all sizes.³⁷ It is noteworthy that in studies of other wide band gap d^0/d^{10} metal oxides such as ZnO, it has been found that the majority of quantum confinement effects originate from an upward shift in the conduction band minimum, and that the top of the valence band energy stays relatively fixed.⁶⁸

From the comparison of (~5 nm) nanosized and larger ceria particles (Fig. 3), it is evident that defects and surface sites play an important role in the absorption spectra, but cause smaller (more defective) particles to have red-shifted absorption onsets compared to large bulk particles.^{6,18} Low coordinate O/OH sites may contribute to the highest energy states in the valence band (Fig. 9).⁶⁹ Theoretical studies of wide band gap group 2 metal oxides find that the frontier orbital energies are located on undercoordinated edge or corner atoms, and in materials exhibiting these effects, band shrinking (quantum confinement effects) is masked by the presence of these size-independent surface energy levels.⁷⁰ Combining a steady Ce 4f energy position, with a surface and/or defect dominated valence band maximum goes some way to explain why there is no observed quantum confinement effect in ceria as both frontier orbital positions remain stable with changing size (Fig. 9).

In the structurally precise Ce-oxo clusters studied here the presence of surface Ce(III) does not change the OMCT absorption onset but does introduce a IVCT transition. Whilst this IVCT signal is very broad, its maxima at ~550 nm (2.3 eV) is

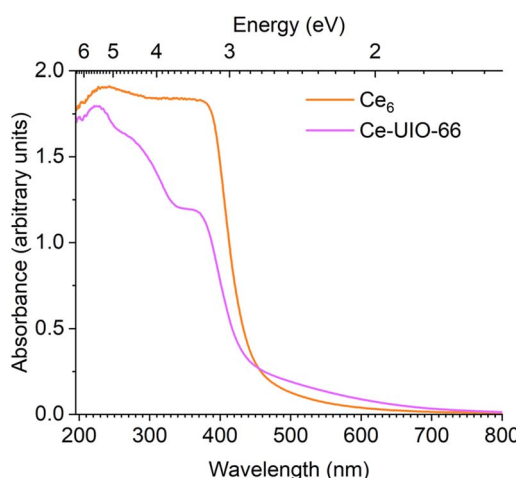


Fig. 8 Diffuse reflectance UV-vis spectra of Ce_6 cluster in comparison to a sample of Ce-UiO-66.

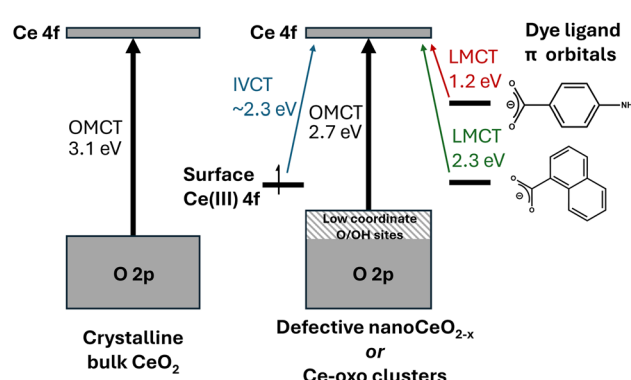


Fig. 9 Diagram proposing the major contributions to the absorption spectra of CeO_2 and (dye-sensitised) mixed valence Ce-oxo clusters. Note that dye ligands may also contribute to LUMO position.



larger than may be expected for moving an electron from a Ce(III) site in $\text{CeO}_{(2-x)}$ to the unoccupied 4f band (~ 1 eV),⁶ which perhaps reflects the specific coordination environments of Ce atoms in these low-symmetry molecules. It is noteworthy that the term ‘oxygen vacancies’ is not a good descriptor for discussing the electronic structure of these mixed valence clusters, as Ce(III) sites are adequately charge balanced by the surface ligand environment. It will be fascinating to see whether targeting this visible-light IVCT can lead to productive photo-redox chemistry. Characterisation of visible excitations in these systems is important as it helps to describe the nature of electronic transitions that contribute to the ‘Urbach tail’ observed in defective ceria nanomaterials and visible absorption in oxygen deficient ceria.^{8,10,12,18} An enhanced understanding of the contributing factors for visible light excitation of ceria materials is essential for their deployment in sunlight driven photocatalytic processes.

Conclusions

The UV/visible spectra of a range of differently sized molecular Ce-oxo clusters from a Ce_3 alkoxide cluster to molecular nanoparticles up to 2.4 nm in core diameter are recorded, and all show consistent OMCT absorption onsets compared to 5 nm $\text{CeO}_{(2-x)}$ particles. This clearly shows that the quantum confinement effect is not observed in ceria particles, and that the frontier unoccupied orbital is best described as a localised 4f orbital on Ce(IV). The presence of Ce(III) sites introduces IVCT transitions across the visible region, and causes the compounds to appear brown-coloured. Introducing dye ligands such as *para*-aminobenzoate or naphthoate, alters the electronic structure such that the frontier orbitals incorporate the organic pi system, and, therefore, the resulting LMCT absorption onset occurs at lower energies (Fig. 9).

A consistent electronic structure for nanoceria down to even the smallest sizes of Ce-oxo clusters is very important for photocatalysis as it shows that abundant blue light (e.g. from sunlight) can be used to excite these structures regardless of their size, noting that solar spectral irradiance drops sharply once into the UV region. Therefore, ultrasmall ceria, which can be designed for solution processability, should be useful for high scale processes that use natural light such as photocatalytic water splitting or in self-cleaning materials.^{40,46} Furthermore, added visible light absorption is possible upon introduction of Ce(III) sites as moderate energy excitation below the band gap allows promotion from Ce(III) to the Ce(IV) core (IVCT). This opens up possibilities for designing materials with ultrasmall ceria particles or Ce-oxo clusters with optimal surface area and atom economy but without reducing their performance in absorbing sunlight.

Data availability

ESI (experimental methods, supporting characterisation and spectra, X-ray crystallography details and analysis).[†] All raw data is deposited in the University of Warwick’s database, WRAP at <https://wrap.warwick.ac.uk/191521/>. CCDC 2418676-

2418679, 2418699–2418701 and 2418814 contain the supplementary crystallographic data for this paper.

Author contributions

S. D. Pike conceived and supervised the project. S. E. Brown conducted all experimental work. Both authors wrote the manuscript.

Conflicts of interest

There are no conflicts to declare.

Acknowledgements

We are grateful for support from the Royal Society for a Royal Society University Research Fellowship for SDP (URF/R1/191458) and Research Grant (RG/R2/232264), and the EPSRC for a studentship for SEB through a Doctoral Training Partnership (DTP) Grant. We thank Prof. Richard Walton, and his research group for constructive discussion and Dr Baiwen Zhao for loan of a sample of Ce-Uo-66.⁶⁷ Thanks to Jack Beall for recording X-ray fluorescence measurements. We acknowledge beamtime at Diamond Light Source (I19 & I11) for X-ray crystallography experiments (CY26668, CY34452, CY39378-1) and thank Gla Sinted for assistance running PXRD samples *via* the Oxford/Warwick Solid-State Chemistry BAG.

References

- 1 T. Montini, *et al.*, Fundamentals and Catalytic Applications of CeO_2 -Based Materials, *Chem. Rev.*, 2016, **116**, 5987–6041, DOI: [10.1021/acs.chemrev.5b00603](https://doi.org/10.1021/acs.chemrev.5b00603).
- 2 S. N. Naidi, *et al.*, Green-synthesized CeO_2 nanoparticles for photocatalytic, antimicrobial, antioxidant and cytotoxicity activities, *J. Mater. Chem. B*, 2021, **9**, 5599–5620, DOI: [10.1039/D1TB00248A](https://doi.org/10.1039/D1TB00248A).
- 3 K. Siposova, *et al.*, Advances in the Study of Cerium Oxide Nanoparticles: New Insights into Antiamyloidogenic Activity, *ACS Appl. Bio Mater.*, 2019, **2**, 1884–1896, DOI: [10.1021/acsabm.8b00816](https://doi.org/10.1021/acsabm.8b00816).
- 4 D. H. Seo, *et al.*, Using a CeO_2 quantum dot hole extraction-layer for enhanced solar water splitting activity of BiVO_4 photoanodes, *Chem. Eng. J.*, 2022, **450**, 137917, DOI: [10.1016/j.cej.2022.137917](https://doi.org/10.1016/j.cej.2022.137917).
- 5 R. G. Agarwal, *et al.*, Nanoparticle O–H Bond Dissociation Free Energies from Equilibrium Measurements of Cerium Oxide Colloids, *J. Am. Chem. Soc.*, 2021, **143**, 2896–2907, DOI: [10.1021/jacs.0c12799](https://doi.org/10.1021/jacs.0c12799).
- 6 R. Schmitt, *et al.*, A review of defect structure and chemistry in ceria and its solid solutions, *Chem. Soc. Rev.*, 2020, **49**, 554–592, DOI: [10.1039/C9CS00588A](https://doi.org/10.1039/C9CS00588A).
- 7 V. Seminko, *et al.*, Mechanism and Dynamics of Fast Redox Cycling in Cerium Oxide Nanoparticles at High Oxidant Concentration, *J. Phys. Chem. C*, 2021, **125**, 4743–4749, DOI: [10.1021/acs.jpcc.1c00382](https://doi.org/10.1021/acs.jpcc.1c00382).



8 Y.-C. Zhang, *et al.*, Role of oxygen vacancies in photocatalytic water oxidation on ceria oxide: experiment and DFT studies, *Appl. Catal., B*, 2018, **224**, 101–108, DOI: [10.1016/j.apcath.2017.10.049](https://doi.org/10.1016/j.apcath.2017.10.049).

9 R. Takada and H. Yao, Optical transitions in nonstoichiometric cerium oxide (CeO_{2-x}) nanoparticles resolved by magnetic circular dichroism (MCD) spectroscopy, *Chem. Phys. Lett.*, 2023, **825**, 140586, DOI: [10.1016/j.cplett.2023.140586](https://doi.org/10.1016/j.cplett.2023.140586).

10 J. S. Pelli Cresi, *et al.*, Ultrafast Formation of Small Polarons and the Optical Gap in CeO_2 , *J. Phys. Chem. Lett.*, 2020, **11**, 5686–5691, DOI: [10.1021/acs.jpclett.0c01590](https://doi.org/10.1021/acs.jpclett.0c01590).

11 T. Duchoň, *et al.*, Covalent *versus* localized nature of 4f electrons in ceria: resonant angle-resolved photoemission spectroscopy and density functional theory, *Phys. Rev. B*, 2017, **95**, 165124, DOI: [10.1103/PhysRevB.95.165124](https://doi.org/10.1103/PhysRevB.95.165124).

12 P. Patsalas, *et al.*, Structure-dependent electronic properties of nanocrystalline cerium oxide films, *Phys. Rev. B: Condens. Matter Mater. Phys.*, 2003, **68**, 035104, DOI: [10.1103/PhysRevB.68.035104](https://doi.org/10.1103/PhysRevB.68.035104).

13 S. D. Kang, *et al.*, Thermopower-conductivity relation for distinguishing transport mechanisms: polaron hopping in CeO_2 and band conduction in SrTiO_3 , *Phys. Rev. B*, 2018, **97**, 235201, DOI: [10.1103/PhysRevB.97.235201](https://doi.org/10.1103/PhysRevB.97.235201).

14 J. J. Plata, *et al.*, Electron Mobility *via* Polaron Hopping in Bulk Ceria: A First-Principles Study, *J. Phys. Chem. C*, 2013, **117**, 14502–14509, DOI: [10.1021/jp402594x](https://doi.org/10.1021/jp402594x).

15 S. Guo, *et al.*, A spectroscopic ellipsometry study of cerium dioxide thin films grown on sapphire by rf magnetron sputtering, *J. Appl. Phys.*, 1995, **77**, 5369–5376, DOI: [10.1063/1.359225](https://doi.org/10.1063/1.359225).

16 R. A. C. Amoresi, *et al.*, CeO_2 Nanoparticle Morphologies and Their Corresponding Crystalline Planes for the Photocatalytic Degradation of Organic Pollutants, *ACS Appl. Nano Mater.*, 2019, **2**, 6513–6526, DOI: [10.1021/acsnano.9b01452](https://doi.org/10.1021/acsnano.9b01452).

17 M. D. Hernández-Alonso, *et al.*, Confinement effects in quasi-stoichiometric CeO_2 nanoparticles, *Phys. Chem. Chem. Phys.*, 2004, **6**, 3524–3529, DOI: [10.1039/B403202K](https://doi.org/10.1039/B403202K).

18 B. Choudhury, *et al.*, Oxygen defects and formation of Ce^{3+} affecting the photocatalytic performance of CeO_2 nanoparticles, *RSC Adv.*, 2014, **4**, 4663–4671, DOI: [10.1039/C3RA44603D](https://doi.org/10.1039/C3RA44603D).

19 T. Edvinsson, Optical quantum confinement and photocatalytic properties in two-, one- and zero-dimensional nanostructures, *R. Soc. Open Sci.*, 2018, **5**, 180387, DOI: [10.1098/rsos.180387](https://doi.org/10.1098/rsos.180387).

20 E. A. Meulenkamp, Synthesis and Growth of ZnO Nanoparticles, *J. Phys. Chem. B*, 1998, **102**, 5566–5572, DOI: [10.1021/jp980730h](https://doi.org/10.1021/jp980730h).

21 J. B. Benedict and P. Coppens, The Crystalline Nanocluster Phase as a Medium for Structural and Spectroscopic Studies of Light Absorption of Photosensitizer Dyes on Semiconductor Surfaces, *J. Am. Chem. Soc.*, 2010, **132**, 2938–2944, DOI: [10.1021/ja909600w](https://doi.org/10.1021/ja909600w).

22 L. Yin, *et al.*, Sonochemical Synthesis of Cerium Oxide Nanoparticles—Effect of Additives and Quantum Size Effect, *J. Colloid Interface Sci.*, 2002, **246**, 78–84, DOI: [10.1006/jcis.2001.8047](https://doi.org/10.1006/jcis.2001.8047).

23 N. S. Arul, *et al.*, Strong quantum confinement effect in nanocrystalline cerium oxide, *Mater. Lett.*, 2011, **65**, 2635–2638, DOI: [10.1016/j.matlet.2011.05.022](https://doi.org/10.1016/j.matlet.2011.05.022).

24 N. W. Pettinger, *et al.*, Photoreductive dissolution of cerium oxide nanoparticles and their size-dependent absorption properties, *Phys. Chem. Chem. Phys.*, 2020, **22**, 5756–5764, DOI: [10.1039/C9CP06579B](https://doi.org/10.1039/C9CP06579B).

25 T. Masui, *et al.*, Characterization of Cerium(IV) Oxide Ultrafine Particles Prepared Using Reversed Micelles, *Chem. Mater.*, 1997, **9**, 2197–2204, DOI: [10.1021/cm970359v](https://doi.org/10.1021/cm970359v).

26 D. Damatov, *et al.*, Redox Reactivity of Colloidal Nanoceria and Use of Optical Spectra as an *In Situ* Monitor of Ce Oxidation States, *Inorg. Chem.*, 2018, **57**, 14401–14408, DOI: [10.1021/acs.inorgchem.8b02598](https://doi.org/10.1021/acs.inorgchem.8b02598).

27 S. M. Laga, *et al.*, Cooperation of cerium oxide nanoparticles and soluble molecular catalysts for alcohol oxidation, *Inorg. Chem. Front.*, 2020, **7**, 1386–1393, DOI: [10.1039/C9QI01640F](https://doi.org/10.1039/C9QI01640F).

28 D. Prieur, *et al.*, Size Dependence of Lattice Parameter and Electronic Structure in CeO_2 Nanoparticles, *Inorg. Chem.*, 2020, **59**, 5760–5767, DOI: [10.1021/acs.inorgchem.0c00506](https://doi.org/10.1021/acs.inorgchem.0c00506).

29 S. V. N. T. Kuchibhatla, *et al.*, Influence of Aging and Environment on Nanoparticle Chemistry: Implication to Confinement Effects in Nanoceria, *J. Phys. Chem. C*, 2012, **116**, 14108–14114, DOI: [10.1021/jp300725s](https://doi.org/10.1021/jp300725s).

30 Y.-C. Huang, *et al.*, Mild Synthesis of Size-Tunable CeO_2 Octahedra for Band Gap Variation, *Chem. Mater.*, 2020, **32**, 2631–2638, DOI: [10.1021/acs.chemmater.0c00318](https://doi.org/10.1021/acs.chemmater.0c00318).

31 S.-H. Wu, *et al.*, Growth of CeO_2 nanocubes showing size-dependent optical and oxygen evolution reaction behaviors, *Dalton Trans.*, 2021, **50**, 15170–15175, DOI: [10.1039/D1DT03150C](https://doi.org/10.1039/D1DT03150C).

32 K. J. Mitchell, *et al.*, Atomically-precise colloidal nanoparticles of cerium dioxide, *Nat. Commun.*, 2017, **8**, 1445, DOI: [10.1038/s41467-017-01672-4](https://doi.org/10.1038/s41467-017-01672-4).

33 B. Russell-Webster, *et al.*, Truly Monodisperse Molecular Nanoparticles of Cerium Dioxide of 2.4 nm dimensions: A $\{\text{Ce}_{100}\text{O}_{167}\}$ Cluster, *Angew. Chem., Int. Ed.*, 2021, **60**, 12591–12596, DOI: [10.1002/anie.202103110](https://doi.org/10.1002/anie.202103110).

34 K. J. Mitchell, *et al.*, Expansion of the Family of Molecular Nanoparticles of Cerium Dioxide and Their Catalytic Scavenging of Hydroxyl Radicals, *Inorg. Chem.*, 2021, **60**, 1641–1653, DOI: [10.1021/acs.inorgchem.0c03133](https://doi.org/10.1021/acs.inorgchem.0c03133).

35 B. Russell-Webster, *et al.*, Phosphorus-based ligand effects on the structure and radical scavenging ability of molecular nanoparticles of CeO_2 , *Dalton Trans.*, 2021, **50**, 15524–15532, DOI: [10.1039/D1DT02667D](https://doi.org/10.1039/D1DT02667D).

36 J. N. Wacker, *et al.*, Reactivity of a Chloride Decorated, Mixed Valant CeIII/IV38–Oxo Cluster, *Inorg. Chem.*, 2022, **61**, 193–205, DOI: [10.1021/acs.inorgchem.1c02705](https://doi.org/10.1021/acs.inorgchem.1c02705).

37 P. Estevenon, *et al.*, From Molecular Oxo-Hydroxo Ce Clusters to Crystalline CeO_2 , *Chem. Mater.*, 2023, **35**, 1723–1734, DOI: [10.1021/acs.chemmater.2c03456](https://doi.org/10.1021/acs.chemmater.2c03456).

38 G. Johnson, *et al.*, Nanocluster superstructures assembled *via* surface ligand switching at high temperature, *Nat. Synth.*, 2023, **2**, 828–837, DOI: [10.1038/s44160-023-00304-8](https://doi.org/10.1038/s44160-023-00304-8).



39 W.-D. Liu, *et al.*, A mixed valence decanuclear cerium-oxo cluster CeIII4CeIV6 for efficient photocurrent response, *Inorg. Chem. Commun.*, 2024, **159**, 111763, DOI: [10.1016/j.inoche.2023.111763](https://doi.org/10.1016/j.inoche.2023.111763).

40 T. Kawakami, *et al.*, Syntheses and Redox Properties of Carboxylate-Ligated Hexanuclear Ce(IV) Clusters and Their Photoinduced Homolysis of the Ce(IV)-Ligand Covalent Bond, *Inorg. Chem.*, 2022, **61**, 20461–20471, DOI: [10.1021/acs.inorgchem.2c03163](https://doi.org/10.1021/acs.inorgchem.2c03163).

41 J. Gosch, *et al.*, Solubility and Stability of Hexanuclear Ce(IV)-O Clusters, *Chem. Mater.*, 2023, **35**, 5876–5885, DOI: [10.1021/acs.chemmater.3c00636](https://doi.org/10.1021/acs.chemmater.3c00636).

42 S. Smolders, *et al.*, A precursor method for the synthesis of new Ce(IV) MOFs with reactive tetracarboxylate linkers, *Chem. Commun.*, 2018, **54**, 876–879, DOI: [10.1039/C7CC08200B](https://doi.org/10.1039/C7CC08200B).

43 M. Lammert, *et al.*, Cerium-based metal organic frameworks with UiO-66 architecture: synthesis, properties and redox catalytic activity, *Chem. Commun.*, 2015, **51**, 12578–12581, DOI: [10.1039/C5CC02606G](https://doi.org/10.1039/C5CC02606G).

44 J. Jacobsen, *et al.*, The chemistry of Ce-based metal-organic frameworks, *Dalton Trans.*, 2020, **49**, 16551–16586, DOI: [10.1039/D0DT02813D](https://doi.org/10.1039/D0DT02813D).

45 Z. Hu, *et al.*, The chemistry and applications of hafnium and cerium(IV) metal-organic frameworks, *Chem. Soc. Rev.*, 2021, **50**, 4629–4683, DOI: [10.1039/D0CS00920B](https://doi.org/10.1039/D0CS00920B).

46 S. Shirase, *et al.*, Cerium(IV) Carboxylate Photocatalyst for Catalytic Radical Formation from Carboxylic Acids: Decarboxylative Oxygenation of Aliphatic Carboxylic Acids and Lactonization of Aromatic Carboxylic Acids, *J. Am. Chem. Soc.*, 2020, **142**, 5668–5675, DOI: [10.1021/jacs.9b12918](https://doi.org/10.1021/jacs.9b12918).

47 X.-P. Wu, *et al.*, Cerium Metal-Organic Framework for Photocatalysis, *J. Am. Chem. Soc.*, 2018, **140**, 7904–7912, DOI: [10.1021/jacs.8b03613](https://doi.org/10.1021/jacs.8b03613).

48 E. E. Ghadim, *et al.*, Rapid synthesis of cerium-UiO-66 MOF nanoparticles for photocatalytic dye degradation, *Dalton Trans.*, 2023, **52**, 11143–11157, DOI: [10.1039/D3DT00890H](https://doi.org/10.1039/D3DT00890H).

49 H. Chen, *et al.*, Functionalized Uio-66(Ce) for photocatalytic organic transformation: the role of active sites modulated by ligand functionalization, *Catal. Sci. Technol.*, 2022, **12**, 1812–1823, DOI: [10.1039/D1CY02344F](https://doi.org/10.1039/D1CY02344F).

50 T. J. Barnes, *et al.*, Synthesis of a nanoscale Cu(II)31-oxo-carboxylate cluster, and effect of Cu-oxo cluster size on visible-light absorption, *Chem. Commun.*, 2023, **59**, 59–62, DOI: [10.1039/D2CC05478G](https://doi.org/10.1039/D2CC05478G).

51 S. Biswas, *et al.*, Highly Localized Charge Transfer Excitons in Metal Oxide Semiconductors, *Nano Lett.*, 2018, **18**, 1228–1233, DOI: [10.1021/acs.nanolett.7b04818](https://doi.org/10.1021/acs.nanolett.7b04818).

52 W. J. Evans, *et al.*, Synthetic and structural studies of a series of soluble cerium(IV) alkoxide and alkoxide nitrate complexes, *Inorg. Chem.*, 1989, **28**, 4027–4034, DOI: [10.1021/ic00320a018](https://doi.org/10.1021/ic00320a018).

53 J. Schläfer, *et al.*, Heterobi- and Trimetallic Cerium(IV) tert-Butoxides with Mono-, Di-, and Trivalent Metals (M = K(I), Ge(II), Sn(II), Pb(II), Al(III), Fe(III)), *Inorg. Chem.*, 2013, **52**, 4002–4010, DOI: [10.1021/ic400030j](https://doi.org/10.1021/ic400030j).

54 V. Mereacre, *et al.*, Homo- and Heterovalent Polynuclear Cerium and Cerium/Manganese Aggregates, *Helv. Chim. Acta*, 2009, **92**, 2507–2524, DOI: [10.1002/hlca.200900192](https://doi.org/10.1002/hlca.200900192).

55 P. L. Roulhac and G. J. Palenik, Bond Valence Sums in Coordination Chemistry. The Calculation of the Oxidation State of Cerium in Complexes Containing Cerium Bonded Only to Oxygen, *Inorg. Chem.*, 2003, **42**, 118–121, DOI: [10.1021/ic025980y](https://doi.org/10.1021/ic025980y).

56 Y. Gao, Y. Zhang, Z. Han, C. Wang, L. Zhang and J. Qiu, Two mixed-valent cerium oxo clusters: synthesis, structure, and self-assembly, *Front. Chem.*, 2024, **12**, 1507834, DOI: [10.3389/fchem.2024.1507834](https://doi.org/10.3389/fchem.2024.1507834).

57 P. Makuła, *et al.*, How To Correctly Determine the Band Gap Energy of Modified Semiconductor Photocatalysts Based on UV-Vis Spectra, *J. Phys. Chem. Lett.*, 2018, **9**, 6814–6817, DOI: [10.1021/acs.jpcllett.8b02892](https://doi.org/10.1021/acs.jpcllett.8b02892).

58 N. Uekawa, *et al.*, Photochromic property of cerium oxide nanoparticles prepared by dialysis of solution of cerium nitrate, *Results Chem.*, 2022, **4**, 100506, DOI: [10.1016/j.rechem.2022.100506](https://doi.org/10.1016/j.rechem.2022.100506).

59 R. E. Sykora, *et al.*, Isolation of Intermediate-Valent Ce(III)/Ce(IV) Hydrolysis Products in the Preparation of Cerium Iodates: Electronic and Structural Aspects of $\text{Ce}_2(\text{IO}_3)_6(\text{OH}_x)$ ($x \approx 0$ and 0.44), *Chem. Mater.*, 2004, **16**, 1343–1349, DOI: [10.1021/cm035147e](https://doi.org/10.1021/cm035147e).

60 Y. K. Gun'ko, *et al.*, First mixed valence cerium-organic trinuclear cluster $[\text{Ce}_3(\text{OBu})_{10}\text{NO}_3]$ as a possible molecular switch: synthesis, structure and density functional calculations, *J. Chem. Soc., Dalton Trans.*, 2002, 1852–1856, DOI: [10.1039/B110247H](https://doi.org/10.1039/B110247H).

61 T. J. N. Obey, *et al.*, A Delocalized Mixed-Valence Dinuclear Ytterbium Complex That Displays Intervalence Charge Transfer, *J. Am. Chem. Soc.*, 2024, **146**, 28658–28662, DOI: [10.1021/jacs.4c12188](https://doi.org/10.1021/jacs.4c12188).

62 M. D. Roy, *et al.*, Intervalence Charge Transfer in Nonbonding, Mixed-Valence, Homobimetallic Ytterbium Complexes, *J. Am. Chem. Soc.*, 2024, **146**, 5560–5568, DOI: [10.1021/jacs.3c13906](https://doi.org/10.1021/jacs.3c13906).

63 C. A. Gould, *et al.*, Ultrahard magnetism from mixed-valence dilanthanide complexes with metal-metal bonding, *Science*, 2022, **375**, 198–202, DOI: [10.1126/science.abl5470](https://doi.org/10.1126/science.abl5470).

64 J. Wang, *et al.*, Ti-based MOFs: new insights on the impact of ligand composition and hole scavengers on stability, charge separation and photocatalytic hydrogen evolution, *Appl. Catal., B*, 2021, **283**, 119626, DOI: [10.1016/j.apcatb.2020.119626](https://doi.org/10.1016/j.apcatb.2020.119626).

65 W. Hou, *et al.*, Understanding charge separation in CdS/Ce-UiO-66-NH₂ heterojunctions for enhanced photocatalytic hydrogen evolution, *Sustainable Energy Fuels*, 2025, **9**, 576–584, DOI: [10.1039/D4SE01473A](https://doi.org/10.1039/D4SE01473A).

66 C. Liu, *et al.*, The defect-modulated Uio-66(Ce) MOFs for enhancing photocatalytic selective organic oxidations, *Rare Met.*, 2025, **44**, 2462–2473, DOI: [10.1007/s12598-024-02693-x](https://doi.org/10.1007/s12598-024-02693-x).

67 B. Zhao, *et al.*, Cerium-Organic Framework Uio-66(Ce) as a Support for Nanoparticulate Gold for Use in Oxidation Catalysis, *Chem.-Asian J.*, 2024, **19**, e202401035, DOI: [10.1002/asia.202401035](https://doi.org/10.1002/asia.202401035).



68 T. J. Jacobsson and T. Edvinsson, Photoelectrochemical Determination of the Absolute Band Edge Positions as a Function of Particle Size for ZnO Quantum Dots, *J. Phys. Chem. C*, 2012, **116**, 15692–15701, DOI: [10.1021/jp302220w](https://doi.org/10.1021/jp302220w).

69 X. Zhang, *et al.*, Environment-Driven Variability in Absolute Band Edge Positions and Work Functions of Reduced Ceria, *J. Am. Chem. Soc.*, 2024, **146**, 16814–16829, DOI: [10.1021/jacs.4c05053](https://doi.org/10.1021/jacs.4c05053).

70 M. A. Zwijnenburg, The effect of particle size on the optical and electronic properties of magnesium oxide nanoparticles, *Phys. Chem. Chem. Phys.*, 2021, **23**, 21579–21590, DOI: [10.1039/D1CP02683F](https://doi.org/10.1039/D1CP02683F).

